

TRUTH OR DELUSION? A POSSIBLE GRAVITATIONAL LENSING INTERPRETATION OF THE ULTRA-LUMINOUS QUASAR SDSS J010013.02+280225.8 AT $z = 6.30$

SEIJI FUJIMOTO^{1,2,3}, MASAMUNE OGURI^{4,5,6}, TOHRU NAGAO⁷, IZUMI TAKUMA^{3,8}, AND MASAMI OUCHI^{1,6,8}

Submitted to ApJ

ABSTRACT

Gravitational lensing sometimes dominates the observed properties of apparently very bright objects. We present morphological properties in the high-resolution (FWHM $\sim 0''.1$) Atacama Large Millimeter/submillimeter Array (ALMA) 1-mm map for an ultra-luminous quasar (QSO) at $z = 6.30$, SDSS J010013.02+280225.8 (hereafter J0100+2802), whose black hole mass M_{BH} is the most massive ($\sim 1.2 \times 10^{10} M_{\odot}$) at $z > 6$ ever known. We find that the continuum emission of J0100+2802 is resolved into a quadruple system within a radius of $0''.2$, which can be interpreted as either multiple dusty star-forming regions in the host galaxy or multiple images due to strong gravitational lensing. The Mg II absorption and the potential Ly α line features have been identified at $z = 2.33$ in the near-infrared spectroscopy towards J0100+2802, and a simple mass model fitting well reproduces the positions and flux densities of the quadruple system, both of which are consistent with the latter interpretation. Although a high-resolution map taken in the Advanced Camera for Survey (ACS) on board *Hubble Space Telescope* (HST) shows a morphology with an apparently single component, in our fiducial lens mass model it can simply be explained by a ~ 50 pc scale offset between the ALMA and HST emission regions. In this case, the magnification factor for the observed HST emission is obtained to ~ 450 , reducing the intrinsic M_{BH} estimate to even below $10^9 M_{\odot}$. The confirmation or the rejection of the gravitational lensing scenario is important for our understanding of the super-massive black holes in the early Universe.

Keywords: galaxies: formation — galaxies: evolution — galaxies: high-redshift

1. INTRODUCTION

The existence of the super-massive black hole (SMBH) in the early Universe (e.g., Wu et al. 2015; Bañados et al. 2018) challenges to the theories (e.g., Volonteri & Rees 2006) of the formation and growth of the black holes (BHs). Luminous quasars (QSOs) at high redshift are massive galaxies hosting the SMBHs in their centers and thus serve a unique laboratory to study the evolution mechanism of the SMBH as well as the earliest phase of galaxy formation and evolution.

In the last two decades, more than 100 $z \sim 6$ QSOs have been discovered through wide-field surveys in the optical–near infrared (NIR) wavelengths (e.g., Jiang et al. 2009, 2016; Willott et al. 2010; Venemans et al. 2013, 2015; Bañados et al. 2016; Matsuoka et al. 2016, 2018). Currently, the most massive BH at $z > 6$ ever known is J0100+2802 at $z = 6.30$

(Wu et al. 2015), originally identified owing to its red optical color with the dataset of the Sloan Digital Sky Survey (SDSS; York et al. 2000), two Micron All Sky Survey (2MASS; Skrutskie et al. 2006) and the Wide-field Infrared Survey Explorer (WISE; Wright et al. 2010). The bolometric luminosity L_{bol} is estimated to be $4.29 \times 10^{14} L_{\odot}$ based on an empirical conversion factor from the luminosity at 3,000 Å, while the BH mass M_{BH} is evaluated to be $1.24 \pm 0.19 \times 10^{10} M_{\odot}$ via the single-epoch virial M_{BH} estimator based on the MgII line (e.g., Vestergaard & Osmer 2009). Although the ten billion solar mass BH at $z = 6.30$ is reproduced under the assumptions of the Eddington-limited accreting rate and the BH seed mass of at least $1,000 M_{\odot}$ by $z = 40$, it is yet to be known whether these assumptions are valid. Moreover, it is also an open question how to lose the angular momentum in the inter-stellar medium (> 100 pc) and keep the Eddington-limited mass transportation to the accretion disk (< 1 pc) around the central BH (e.g., Sugimura et al. 2018) under the strong feedback effect (e.g., Park et al. 2017; Latif et al. 2018).

The Atacama Large Millimeter / submillimeter Array (ALMA) enables us to investigate the star-forming properties of the SMBH host galaxies at $z \sim 6$ via the far-infrared fine-structure lines, such as [C II] 158 μm and [O III] 88 μm , and the dust continuum emission (e.g., Wang et al. 2013; Decarli et al. 2018; Venemans et al. 2018; Walter et al. 2018; Hashimoto et al. 2018). These ALMA studies reveal that the SMBH host galaxies at $z \sim 6$ have intense star-formation rates of $\sim 100 - 3000 M_{\odot} \text{yr}^{-1}$. The intense star formation may cause the turbulence and contribute to the angular momentum dissipation in the inter-stellar medium (e.g., Kawakatu & Wada

sfseiji@icrr.u-tokyo.ac.jp

¹ Institute for Cosmic Ray Research, The University of Tokyo, Kashiwa, Chiba 277-8582, Japan

² Research Institute for Science and Engineering, Waseda University, 3-4-1 Okubo, Shinjuku, Tokyo 169-8555, Japan

³ National Astronomical Observatory of Japan, 2-21-1, Osawa, Mitaka, Tokyo, Japan

⁴ Research Center for the Early Universe, University of Tokyo, 7-3-1 Hongo, Bunkyo-ku, Tokyo 113-0033, Japan

⁵ Department of Physics, University of Tokyo, 7-3-1 Hongo, Bunkyo-ku, Tokyo 113-0033, Japan

⁶ Kavli Institute for the Physics and Mathematics of the Universe (Kavli IPMU, WPI), University of Tokyo, Chiba 277-8583, Japan

⁷ Research Center for Space and Cosmic Evolution, Ehime University, 2-5 Bunkyo-cho, Matsuyama, Ehime 790-8577, Japan

⁸ Department of Astronomical Science, Graduate University for Advanced Studies (SOKENDAI), 2-21-1 Osawa, Mitaka, Tokyo 181-8588, Japan

2009; Izumi et al. 2016). The size, structure, and dynamics of these star-forming regions in the SMBH host galaxies are thus helpful probes to investigate the mass accretion to the SMBH under the star-forming activities of their host galaxies. However, the majority of these ALMA studies do not resolve the host galaxy structure due to the moderate angular resolution of $\sim 1''0$.

In this paper, we investigate the detailed structure of the host galaxy of J0100+2802 with the high-resolution ($\sim 0''.1$) ALMA Band 6 data. Since J0100+2802 is the representative of the SMBH in the early Universe as the most massive BH ever known at $z > 6$, this is an essential step to understand the spatially-resolved star-forming nature around the early SMBHs. The structure of this paper is as follows. The ALMA observations and the data reduction are described in Section 2. Section 3 outlines the data analysis and interpretation. In Section 4, we discuss the physical properties of J0100+2802. A summary of this study is presented in Section 5.

Throughout this paper, we assume a flat universe with $\Omega_m = 0.3$, $\Omega_\Lambda = 0.7$, $\sigma_8 = 0.8$, and $H_0 = 70 \text{ km s}^{-1} \text{ Mpc}^{-1}$. We use magnitudes in the AB system (Oke & Gunn 1983).

2. DATA & REDUCTION

Observations were carried out on 2016 September 4 in the cycle 4 program (PI: X. Fan; see Wang et al. 2019), using 44 antennas with the projected baselines ranging from 15 m to 2.5 km. The available 7.5 GHz bandwidth with four spectral windows was centered at an observed frequency of 239.8 GHz (i.e., $\sim 1.25 \text{ mm}$). J2253+1608 and J0238+1636 were observed as the flux calibrator, while J2253+1608 and J0237+2848 were used for the bandpass calibrator. Phase calibration was generally performed by using observations of J0057+3021. The total on-source time was $\sim 74 \text{ min}$.

We reduce the ALMA data with the Common Astronomy Software Applications package version 4.7.0 (CASA; McMullin et al. 2007) in the standard manner with the scripts provided by the ALMA observatory. For further data analyses, we use the CASA version 5.4.0. The continuum images are produced with all of the bands by the CLEAN algorithm with the *tclean* task. The CLEAN boxes are set at the peak pixel positions with $S/N \geq 5$ in the auto mode, and the CLEAN routines are proceeded down to the 3σ level. The final natural-weighted image is characterized by a synthesized beam size of $0''.29 \times 0''.15$ and the rms noise level of $16 \mu\text{Jy}/\text{beam}$. We also produced a briggs-weighted maps with the robust parameter of 0.5 and 0.2 whose final synthesized beam sizes are $0''.23 \times 0''.12$ and $0''.21 \times 0''.09$. We refer to the natural-, the briggs- (robust = 0.5), the briggs-weighted (robust = 0.2) maps as “LR”, “MR”, and “HR” maps, respectively. Here we do not use the uniform-weighted continuum map to obtain reliable results with secure signal-to-noise ratios (SNRs). Note that the imaging parameter of the MR map is the same as the continuum map produced in Wang et al. (2019), and we confirm that the same morphology is reproduced in the MR map as the previous works (see Figure 1 in Wang et al. 2019).

3. ANALYSIS & INTERPRETATION

3.1. ALMA

Table 1
Component Summary

Comp.	R.A. (J2000)	Decl. (J2000)	S_{obs} (mJy)	SNR	
(1)	(2)	(3)	(4)	(5)	
Total	1:00:13.026	+28:02:25.81	1.3	21	
	$\Delta\alpha$ (")	$\Delta\delta$ (")	$S_{\text{obs,peak}}$ (mJy/beam)	μ	
	(5)	(6)	(7)	(8)	
AID1	+0.02	-0.05	0.19	10	19.6
AID2	-0.01	+0.12	0.17	8.9	15.2
AID3	-0.13	-0.02	0.14	7.4	13.9
AID4	-0.22	+0.16	0.10	5.4	9.7

Note. — (1) Name of the components. (2) Coordinate of the 1-mm continuum emission evaluated with the peak pixel position. (3) Flux density estimated with the aperture diameter of $0''.8$. (4) Signal-to-noise ratio at the peak. (5) R.A. offset from (1). (6) Decl. offset from (1). (7) Peak pixel value for each component. (8) Magnification factor at the peak estimated with the fiducial mass model.

In Figure 1, we show the LR, MR, and HR maps of J0100+2802. In the LR map, a continuum emission is clearly detected with the 21σ level at the peak. The total flux density is estimated to be 1.3 mJy with an aperture diameter of $0''.8$, which is consistent with the estimate in Wang et al. (2019). The position at the peak and the total flux density are summarized in Table 1.

In the HR map, on the other hand, the continuum emission is resolved into multiple peaks. We identify four peaks with the positive counts above the 5.0σ level that are located within a radius of $\sim 0''.2$. We refer to these four components from bright to faint as AID1, AID2, AID3, and AID4. In Table 1, we summarize the peak counts, SNRs, and the positions for these four components. The sum of the peak counts of the four components reaches 0.6 mJy that corresponds to $\sim 46\%$ ($= 0.6/1.3$) of the total flux density. This suggests that about half of the continuum emission is resolved in the HR map. Note that no negative peaks are detected above the -4.0σ level in the HR map, indicating that these four components are real.

One interpretation for these four components is that they are quadruple images due to strong gravitational lensing effect (e.g., Magain et al. 1988). In the top panel of Figure 2, we show the major absorption line features at $z = 2.33$ in the optical-NIR spectroscopy of J0100+2802 reported in Wu et al. (2015). This suggests existence of the foreground object that may affect the brightness of J0100+2802 via gravitational lensing effect. In fact, the bottom panel of Figure 2 shows the possible Ly α line emission at $z = 2.33$ with the 5.3σ level that we identify in the latest optical-NIR spectroscopy with VLT/Xshooter from the ESO archive (PI: M. Pettini; see Becker et al. 2019).

To test whether the four components identified in the HR map can indeed be explained by strong gravitational lensing, we construct a mass model with the parametric gravitational lensing package GLAFIC (Oguri 2010). Here we fix the lens redshift at $z = 2.33$ where the possible foreground object is identified. The mass model consists of a singular isothermal ellipsoid (SIE) and an external shear. We adopt no priors on the centroid of the SIE, while we add a Gaussian prior on the amplitude of the

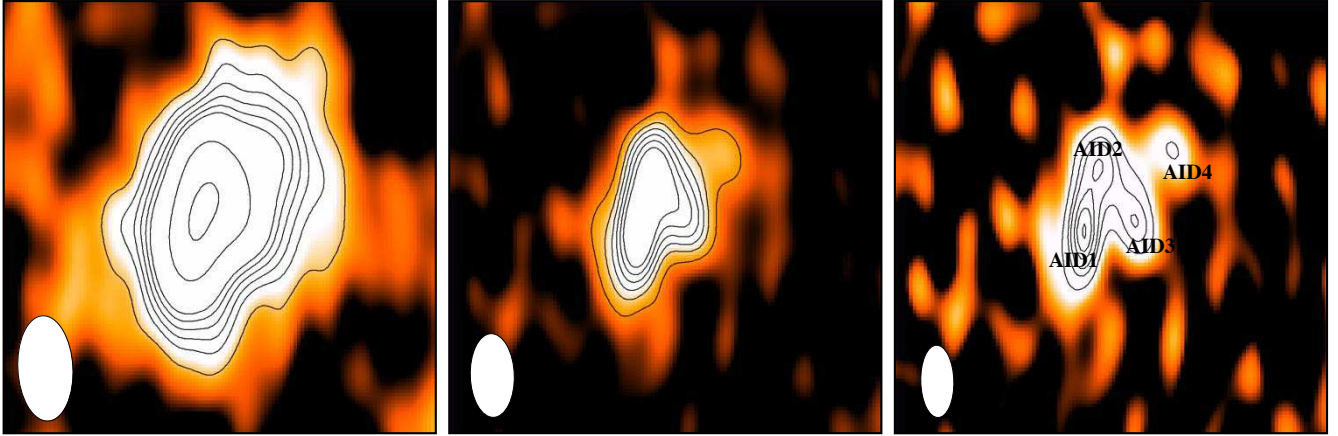


Figure 1. ALMA $1''.2 \times 1''.2$ images of J0100+2802. The LR (natural-weighted), MR (briggs-weighted, robust = 0.5), and HR (briggs-weighted, robust = 0.2) maps are presented from left to right. The black contour denotes the 5σ , 6σ , 7σ , 8σ , 9σ , 10σ , 15σ , and 20σ levels. The ALMA synthesized beam is presented at the bottom left. We confirm that the MR map shows the consistent morphology in the previous study (see Figure 1 in Wang et al. 2019).

external shear of $\gamma = 0.05 \pm 0.05$. The flux errors are assumed to be 10 %. The approximate positional uncertainty of the ALMA map Δp in milliarcsec is given by

$$\Delta p = \frac{70000}{\nu * B * \sigma}, \quad (1)$$

where σ is the peak SNR, ν is the observing frequency in GHz, and B is the maximum baseline length in kilometers (ALMA technical handbook⁹). For a peak with SNR = 5 in our ALMA maps, we obtain Δp of $\sim 0''.02$. Due to the large elongation of the ALMA beam shape, we conservatively adopt the positional error of $0''.03$. After the fitting routine for the four peak positions in the HR map, we obtain the best-fit mass model with the χ^2 over the degree of freedom of 6.11/3. With this fiducial lens mass model, the Einstein radius is $0''.14$ which corresponds to the velocity dispersion of 121 km s^{-1} at the lens redshift of 2.33. We list the magnification factors for the four components in Table 1. The best-fitting mass model predicts the total magnification of ~ 58 for the ALMA source, although given the relatively large positional uncertainty the uncertainty of the lens mass model is also relatively large, with the total magnification range of $\sim 18 - 117$ at 2σ level. Since the purpose of this paper is to present a possibility of the gravitational lensing interpretation rather than the full exploration of the lens mass model, in what follows we focus only on our best-fitting mass model and adopt it as our fiducial model.

Figure 3 presents the positions (left panel) and intrinsic flux densities (right panel) of the four components predicted by our fiducial mass model. In the left panel, the red crosses and triangles show the positions of the four components in the observed and the model maps, respectively. We find that all the four positions are consistent within the errors. In the right panel, the dashed line presents the average value of the intrinsic flux densi-

ties for the four components. We find that the intrinsic flux densities of all four components agree with the average value within the errors. These results quantitatively support that the four components can be explained by multiple images due to strong gravitational lensing.

3.2. Comparison with HST

We compare the morphology in the ALMA HR map with a high-resolution data of the *Hubble Space Telescope* (HST) Advanced Camera for Surveys (ACS) in F850LP (PSF $\sim 0''.1$). In the left panel of Figure 4, we present the HST/F850LP map for J0100+2802 obtained from the final flat-field and flux calibrated science products in the Hubble Legacy Archive (PI: X. Fan). For comparison, we also show the contours of the ALMA emission in the HR map. The astrometry between HST and ALMA is corrected based on the GAIA DR2 catalog (Gaia Collaboration et al. 2018). Interestingly, we find that the morphology of the HST emission appears to consist of a single component, in marked contrast to the ALMA emission. Since the HST and ALMA emissions trace the accretion disk around the central SMBH and the dusty star-forming region in the host galaxy, respectively, the following two possibilities arise to explain the different morphologies of J0100+2802 in the HST and ALMA maps: 1) an offset between the HST and ALMA emission regions in the source plane causes the difference in gravitational lensing effects and produces the different morphologies in the image plane. 2) the four components in the ALMA map represent multiple dusty star-forming regions in the host galaxy or a dusty on-going merging system, rather than multiple images due to strong gravitational lensing, where these star-forming regions are unseen in the HST map due to the dust extinction and the large contrast to the bright emission from the accretion disk.

We investigate whether the possibility of 1) is feasible with our fiducial best-fit mass model. In the middle and right panels of Figure 4, we present the caustics and the critical curve of our fiducial mass model (Section 3.1). We find that our fiducial mass model can reproduce the

⁹ Section 10.5.2: <https://almascience.nao.ac.jp/documents-and-tools/cycle7/alma-technical-handbook>

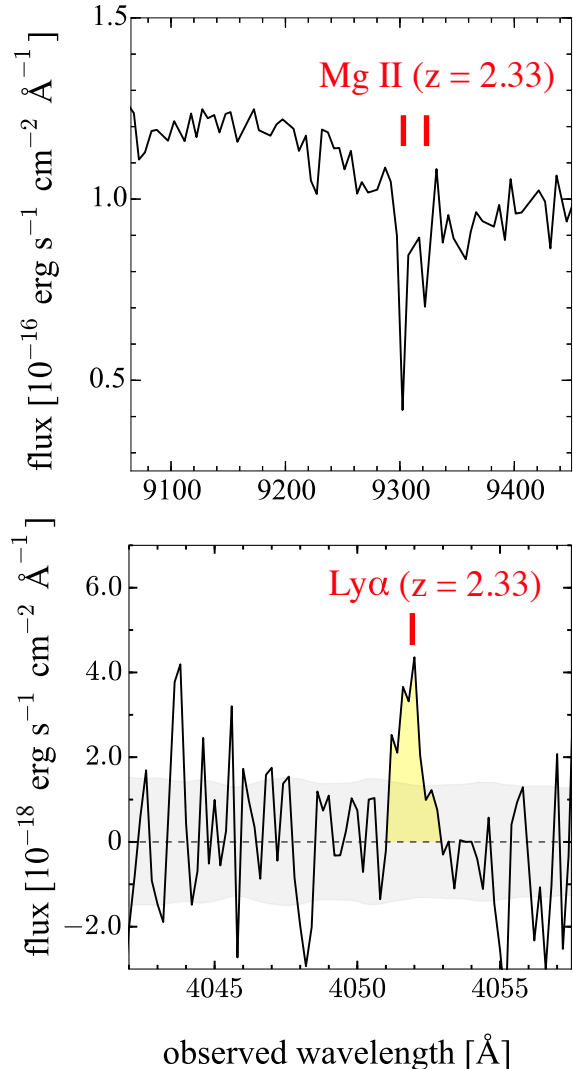


Figure 2. **Top:** Absorption line features in the optical–NIR spectroscopy of J0100+2802 taken from Wu et al. (2015). The Mg II absorption doublets have been identified at $z = 2.33$. **Bottom:** Possible Ly α line emission at $z = 2.33$ with the 5.3σ level identified in the weighted-average spectrum of the latest VLT/Xshooter data in the ESO archive. The gray shaded area represents the 1σ flux uncertainty.

morphology of the apparently single component in the HST map, if the position of the HST emission in the source plane is close to the cusp of the caustics. As an example, in Figure 4 we show a possible position of the HST emission in the source plane (open blue triangle; middle panel) and the corresponding quadruple images in the image plane (filled blue triangle; right panel). We refer to the quadruple lens HST objects from bright to faint as HID1, HID2, HID3, and HID4. In this case, HID1, HID2, and HID3 are produced within a scale below the angular resolution of HST and are not resolved in the observed HST map. Since the sum of HID1, HID2, HID3 is over 100 times brighter than HID4, the HST emission appears as a single-like component in the observed HST map. The offsets among HID1, HID2, and HID3 can be even smaller if the position of the HST

emission in the source plane is located closer to the cusp of the caustics. These results suggest that the possibility of 1) is indeed feasible. Note that the ALMA and HST emission in these cases have the offset of the ~ 50 pc scale in the source plane that is reasonably smaller than the entire host-galaxy scale (\sim kpc).

To quantitatively test the possibility of 1), we also carry out a simulation by making mock HST maps for different separations among HID1, HID2, and HID3. First, we identify isolated and unsaturated stars with SExtractor version 2.5.0 (Bertin & Arnouts 1996) and evaluate the PSF of the HST map. The FWHM of the PSF is estimated to be $0.''103 \pm 0.''003$, where the central and error values are defined by the median and the standard deviation of the individual stars, respectively. Second, we make a mock HST map for the single-like component by injecting three PSFs at the positions of HID1, HID2, and HID3. Since the position of the HST emission in the source plane is sufficiently close to the cusp of the caustics, our fiducial mass model shows that the magnification factors among HID1, HID2, and HID3 maintain a \sim two-one-one ratio and that the positions of HID2 and HID3 are almost symmetry relative to HID1 along the line with the critical curve. We thus fix the brightnesses of these three PSFs at the two-one-one ratio and assume that the positions of HID2 and HID3 keep the same distance from HID1. Here we refer to the distance between HID1 and HID2 (= HID1 and HID3) as l . Finally, we measure the FWHM values for the single-like component in the mock HST map as a function of l .

In Figure 5, we show the simulation results. The gray shaded region denotes the FWHM of the PSF including the uncertainty. For comparison, we also present the FWHM for J0100+2802 in the observed HST map that is estimated to be $0.''113$ (red dashed line). We find that the FWHM of J0100+2802 exceeds that of the PSF, suggesting that the HST emission of J0100+2802 is not a point source. We also find that the FWHM of J0100+2802 corresponds to the simulation results with $l = 0.''04$. In other words, the apparently single component in the HST map can be explained by the merging multiple images HID1, HID2, and HID3 with separation $l = 0.''04$. These results indicate that the possibility of 1) is still consistent with the data. In the case of $l = 0.''04$, our fiducial mass model predicts the total magnification factor of ~ 450 for the quadruple images in the HST map.

4. DISCUSSION

The ALMA high-resolution map resolves the dust emission from J0100+2802 into four components whose positions and flux densities are explained by the gravitational lensing effect (Section 3.1). In contrast to the ALMA results, the high-resolution data of HST/F850LP shows the different morphology with an apparently single component, but the detail morphological analysis with our fiducial lens mass model shows that it is possible to produce quadruple lens images that are consistent with the observed morphology in the HST map if we allow an offset between ALMA and HST emission regions (Section 3.2). Although we cannot draw definitive conclusion between the two possibilities of 1) the quadruply imaged lens system and 2) the multiple dusty star-forming system for J0100+2802 without further high-resolution ob-

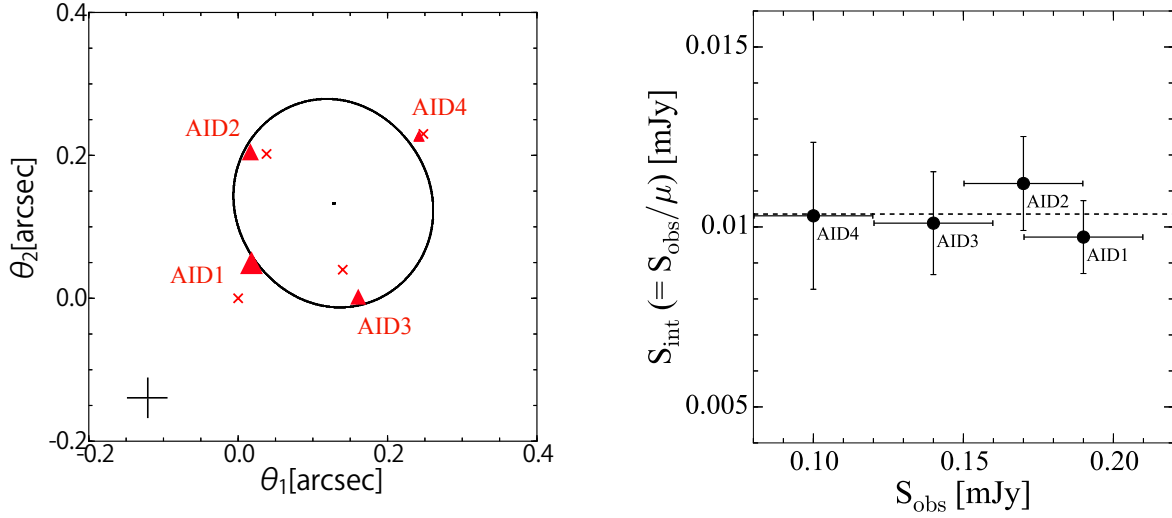


Figure 3. Simple mass model fitting results for positions and flux densities of the four components identified in the ALMA HR map. **Left:** The red crosses and triangles show the peak positions of the four components in the observed and the model maps, respectively. The size difference among the red triangles correspond to the ratio of the magnification factors of the four components in our model. The black curve denotes the critical curve. The error scale used in the fitting is presented at the bottom left. The center of the coordinate is defined at the position of AID1. **Right:** The observed (S_{obs}) and intrinsic (S_{int}) flux densities of the four components. The dashed line presents the average value of the intrinsic flux densities for the four components.

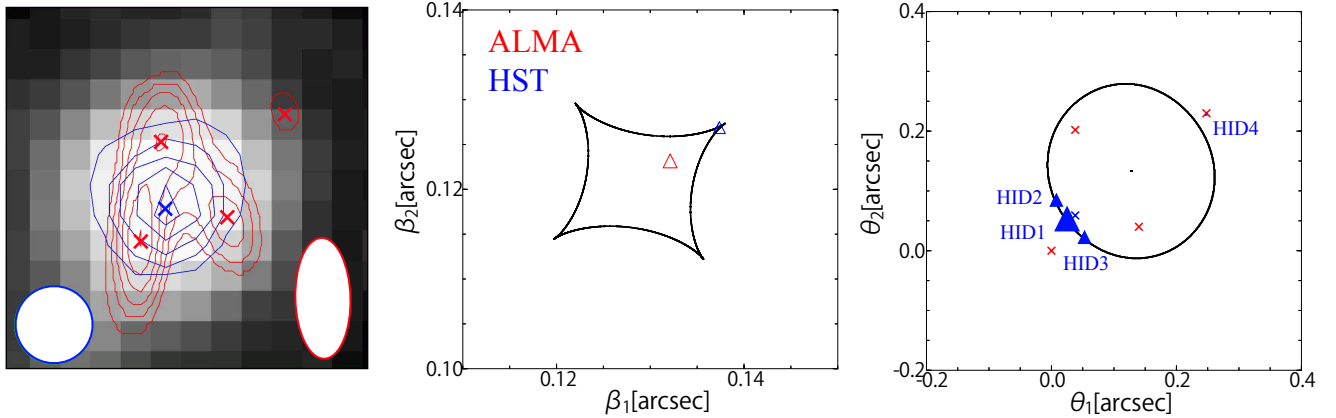


Figure 4. **Left:** The HST/F850LP $0.''6 \times 0.''6$ image for J0100+2802. The blue and red contours denote the continuum emission identified in the HST/F850LP and the ALMA HR maps, respectively. The crosses indicate the peak positions of these emission. The PSFs of the HST and ALMA maps are presented in the bottom left and right, respectively. **Middle:** The continuum peak positions in the source plane. The red open triangle indicates the best-fit position of the ALMA continuum emission in the simple mass model fitting (Section 3.1), and the blue open triangle shows a possible position of the HST continuum emission. The black line is the caustics. **Right:** The continuum peak positions in the image plane. The red and blue crosses are assigned in the same manner as the left panel. The blue triangles denote a possible peak positions of the HST emission in the resolution-free map predicted with our fiducial mass model, if the HST emission originates near from the cusp of the caustic in the source plane. The size difference among the triangles correspond to the ratio of the magnification factors of the four components in our fiducial mass model. The black line denotes the critical curve. In the middle and right panels, the same coordinate system is assigned as the left panel of Figure 3.

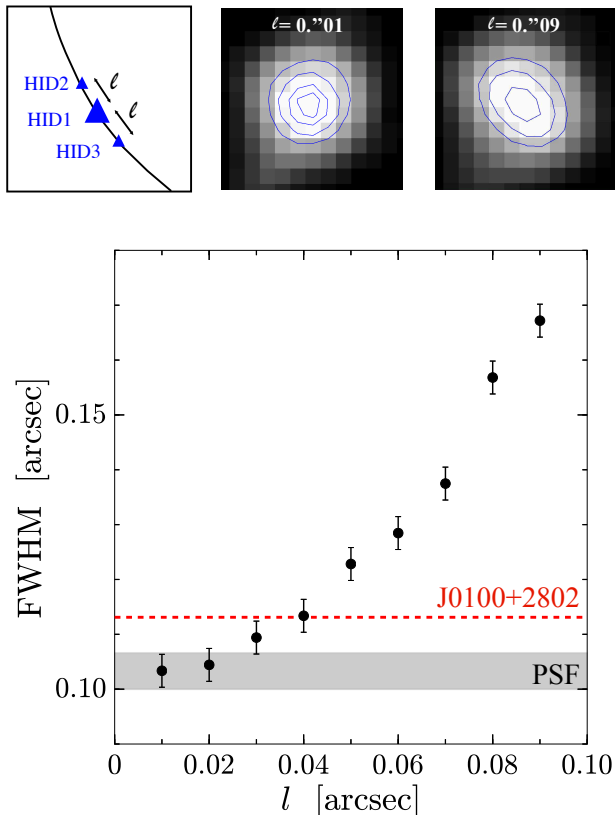


Figure 5. Simulation results of the mock HST map for the single-like component. **Top:** Schematic overview of the simulations. The definition of l and the mock HST maps in the cases of $l = 0.''01$ and $l = 0.''09$ are presented from left to right. **Bottom:** The black circles indicate the FWHM measurements as a function of l . The gray shaded region denotes the FWHM of the PSF estimated from the isolated and unsaturated stars, where the shade width is the uncertainty of the estimate. The red dashed line is the FWHM of J0100+2802 in the observed HST map. We use the uncertainty of the PSF as the error-bar scale of the black circles.

servations, in this section we focus on the possibility of 1) and discuss the intrinsic physical property of J0100+2802 in this scenario.

In the case that the positions of HID1, HID2, and HID3 are very close with $l = 0.''04$, our fiducial lens mass model estimates the total magnification factor of ~ 450 for the quadruple images. The characteristic of J0100+2802 has been measured by the ground-based telescopes at the optical-NIR wavelengths (Wu et al. 2015) whose angular resolutions do not resolve the structure. Therefore, the previous measurements can be affected by the magnification factor of ~ 450 .

The virial M_{BH} estimator based on the Mg II line (e.g., Vestergaard & Osmer 2009) is given by

$$M_{\text{BH}} = 10^{6.86} \left(\frac{\lambda L_{\lambda,3000}}{10^{44} \text{erg s}^{-1}} \right)^{0.5} \left(\frac{\text{FWHM}_{\text{MgII}}}{\text{km s}^{-1}} \right)^2, \quad (2)$$

where $\lambda L_{\lambda,3000}$ is the rest-frame UV luminosity at 3000 Å wavelength and $\text{FWHM}_{\text{MgII}}$ is the full-width-half-maximum of the Mg II line in the spectrum. If we apply the total magnification correction to the UV luminosity in Equation 2, the intrinsic M_{BH} estimate is decreased

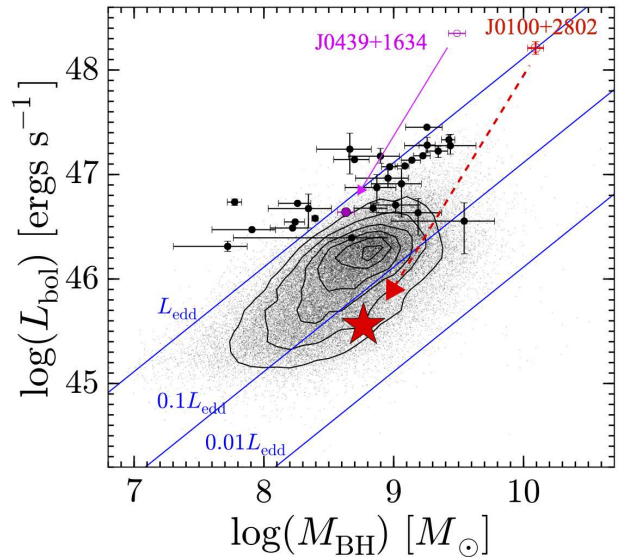


Figure 6. Distribution of bolometric luminosity L_{bol} and BH mass M_{BH} estimated from Mg II line among QSOs. The red open circle indicates the apparent property of J0100+2802 (Wu et al. 2015), while the red star denotes the potential intrinsic property after the gravitational lensing correct. For comparison, the magenta open and filled circles present the apparent and intrinsic properties of J0439+1634 that is identified as a gravitationally lensed QSO at $z = 6.42$ (Fan et al. 2019). The black circles are other QSOs at $z \gtrsim 6$ (Mortlock et al. 2011; Mazzucchelli et al. 2017; Bañados et al. 2018), and the grey dots and black contours are the distribution of the SDSS QSOs at $z = 0 - 2$ (Shen et al. 2011). The blue lines present fractions of the Eddington luminosity.

by a factor of ~ 17.3 . In Figure 6, we show the intrinsic values of L_{bol} and M_{BH} of J0100+2802 after the total magnification correction. We find that J0100+2802 falls in the area within the distribution of low-redshift SDSS QSOs, and that the M_{BH} value is decreased even below $10^9 M_{\odot}$. These results indicate that the gravitational lensing effect has a significant potential to change our understanding of the nature of the most massive SMBH at $z > 6$.

Note that we cannot rule out the possibility of 2). Recent ALMA observations reveal the overdensity of companion galaxies around the high- z luminous QSOs (e.g., Decarli et al. 2017; Trakhtenbrot et al. 2017). The follow-up ALMA high-resolution observations also report the existence of the nearby on-going mergers around the $z > 6$ QSOs (Venemans et al. 2019; Bañados et al. 2019). The existence of the on-going mergers and/or the ISM environment harboring the multiple dusty star-forming regions in J0100+2802 will be definitely interesting and provide us with important insights to understand the rapid growth of the most massive SMBH in the early Universe. However, the Mg II absorption and the Ly α line features at $z = 2.33$ in the optical-NIR spectroscopy implies the existence of the foreground galaxy that can cause gravitational lensing effect. Moreover, recent HST observations report that another SDSS QSO at $z = 6.34$, J0439+1634, known as the brightest QSO ($L_{\text{bol}} = 5.9 \times 10^{14} L_{\odot}$) at $z > 6$, is resolved into multiple objects with the existence of the nearby, low-luminous galaxy at the photometric redshift $z \sim 0.7$ (Fan et al. 2019; Pacucci & Loeb 2019). The authors ar-

gue that the magnification factor is estimated to be ~ 50 in their best-fit mass model that dramatically changes the intrinsic physical properties of J0439+1634 such as L_{bol} and M_{BH} . Importantly, the g , r , i -band AB magnitudes of the foreground galaxy of J0439+1634 are ~ 23 – 25 mag that are lower than the SDSS limiting magnitudes ($5\sigma \sim 21$ – 22 mag) and thus negligible in the color diagnostics used for the QSO selection. Our and recent results suggest a possibility that a number of other bright QSOs at $z \gtrsim 6$ are caused by the gravitational lensing effect by such low-luminous, but nearby foreground galaxies, even in the case that the morphology appears to consist of a single component. We note that such large number of strong gravitational lensing among the apparently bright high-redshift QSOs are naturally explained by the magnification bias effect (Turner 1980), which tends to dominate at the bright end of any class of sources (e.g., Irwin et al. 1998; Wyithe & Loeb 2002; Negrello et al. 2010; Quimby et al. 2014). The systematic high-resolution observations towards bright QSOs at $z > 6$ are essential with ALMA, HST, and upcoming JWST.

5. SUMMARY

In this paper, we study the detailed morphology of the ALMA 1-mm continuum emission from the bright QSO at $z = 6.30$, J0100+2802, that is known to contain the most massive BH at $z > 6$ so far identified. In the high-resolution map, the emission is resolved into four components. We compare the ALMA results with the HST/F850LP data and investigate whether these four components are caused by the gravitational lensing effect, which potentially has a significant impact on the estimate of intrinsic physical properties of J0100+2802. The major findings of this paper are summarized below.

1. We identify a clear continuum detection from J0100+2802 with the 21σ level at the peak in the natural-weighted map, where the total flux density is estimated to be 1.3 mJy with the aperture diameter of $0''.8$. In the briggs-weighted map (robust = 0.2), the spatial resolution is improved about 40% and the continuum emission is resolved into four components whose peak counts are all above the 5σ level.
2. We detect a possible Ly α line emission at the 5.3σ level at $z = 2.33$ in the latest optical–NIR spectroscopy with VLT/Xshooter from the ESO archive, which is consistent with the Mg II absorption line feature at $z = 2.33$ reported in the previous studies (Wu et al. 2015). We construct a lens mass model assuming strong lensing by a galaxy at $z = 2.33$ to find that a simple mass model well reproduces the peak positions and flux densities for the four components identified in the ALMA map.
3. The HST/F850LP map for J0100+2802 shows a morphology with an apparently single component, in marked contrast to the ALMA results. We discuss the following two possibilities for the difference in morphologies of J0100+2802 in the ALMA and HST maps: 1) an intrinsic offset between the ALMA and HST emission in the source plane causes the different gravitational lensing effects

and produces the different morphologies in the image plane. 2) the four components in the ALMA map represent multiple dusty star-forming regions, rather than strongly lensed multiple images, where these star-forming regions are unseen in the HST map due to the dust extinction and the large contrast to the bright emission from the accretion disk.

4. Assuming the possibility of 1), our fiducial best-fit lens mass model predicts the magnification factor of ~ 450 for the observed HST emission. After the correction of gravitational lensing magnification, the intrinsic L_{bol} and M_{BH} relation falls in the area within the distribution of the low-redshift SDSS QSOs, and the M_{BH} measurement is decreased even below $10^9 M_{\odot}$. Our results suggest that the gravitational lensing effect has a significant potential to change our understanding of the most massive SMBH in the early Universe, and therefore should be explored further by future observations.

We are grateful to Nozomu Kawakatsu for organizing the productive workshop that made us start this study. We appreciate Shiro Mukae, Yoshiaki Ono, Ken Mawatari, Hiroshi Nagai, Yoichi Tamura, and Akio Inoue for providing us the helpful advice on analyzing the data. This paper makes use of ALMA data: ADS/JAO.ALMA #2015.1.00692.S. ALMA is a partnership of the ESO (representing its member states), NSF (USA) and NINS (Japan), together with NRC (Canada), MOST and ASIAA (Taiwan), and KASI (Republic of Korea), in cooperation with the Republic of Chile. The Joint ALMA Observatory is operated by the ESO, AUI/NRAO, and NAOJ. This study is supported by World Premier International Research Center Initiative (WPI Initiative), MEXT, Japan, and KAKENHI (15H02064, 16J02344, 16K17670, 17H01114, 17K14247, 18K03693) Grant-in-Aid for Scientific Research (A) through Japan Society for the Promotion of Science (JSPS), Grant-in-Aid for Scientific Research (C) through JSPS, Grant-in-Aid for Scientific Research on Innovative Areas, and the Grant-in-Aid for JSPS Research Fellow, and NAOJ ALMA Scientific Research Grant Number 2016-01A. S.F. is supported by the ALMA Japan Research Grant of NAOJ Chile Observatory NAOJ-ALMA-231.

REFERENCES

- Bañados, E., Venemans, B. P., Decarli, R., et al. 2016, *ApJS*, 227, 11
- Bañados, E., Venemans, B. P., Mazzucchelli, C., et al. 2018, *Nature*, 553, 473
- Bañados, E., Novak, M., Neeleman, M., et al. 2019, *ApJ*, 881, L23
- Becker, G. D., Pettini, M., Rafelski, M., et al. 2019, arXiv e-prints, arXiv:1907.02983
- Bertin, E., & Arnouts, S. 1996, *A&A*, 117, 393
- Decarli, R., Walter, F., Venemans, B. P., et al. 2017, *Nature*, 545, 457
- . 2018, *ApJ*, 854, 97
- Fan, X., Wang, F., Yang, J., et al. 2019, *ApJ*, 870, L11
- Gaia Collaboration, Brown, A. G. A., Vallenari, A., et al. 2018, *A&A*, 616, A1
- Hashimoto, T., Inoue, A. K., Tamura, Y., et al. 2018, arXiv e-prints, arXiv:1811.00030
- Irwin, M. J., Ibata, R. A., Lewis, G. F., & Totten, E. J. 1998, *The Astrophysical Journal*, 505, 529
- Izumi, T., Kawakatu, N., & Kohno, K. 2016, *ApJ*, 827, 81
- Jiang, L., Fan, X., Bian, F., et al. 2009, *AJ*, 138, 305

- Jiang, L., McGreer, I. D., Fan, X., et al. 2016, *ApJ*, 833, 222
Kawakatu, N., & Wada, K. 2009, *ApJ*, 706, 676
Latif, M. A., Volonteri, M., & Wise, J. H. 2018, *MNRAS*, 476, 5016
Magain, P., Surdej, J., Swings, J. P., Borgeest, U., & Kayser, R. 1988, *Nature*, 334, 325
Matsuoka, Y., Onoue, M., Kashikawa, N., et al. 2016, *ApJ*, 828, 26
Matsuoka, Y., Iwasawa, K., Onoue, M., et al. 2018, *ApJS*, 237, 5
Mazzucchelli, C., Bañados, E., Venemans, B. P., et al. 2017, *ApJ*, 849, 91
McMullin, J. P., Waters, B., Schiebel, D., Young, W., & Golap, K. 2007, in *Astronomical Society of the Pacific Conference Series*, Vol. 376, *Astronomical Data Analysis Software and Systems XVI*, ed. R. A. Shaw, F. Hill, & D. J. Bell, 127
Mortlock, D. J., Warren, S. J., Venemans, B. P., et al. 2011, *Nature*, 474, 616
Negrello, M., Hopwood, R., De Zotti, G., et al. 2010, *Science*, 330, 800
Oguri, M. 2010, *PASJ*, 62, 1017
Oke, J. B., & Gunn, J. E. 1983, *ApJ*, 266, 713
Pacucci, F., & Loeb, A. 2019, *ApJ*, 870, L12
Park, K., Wise, J. H., & Bogdanović, T. 2017, *ApJ*, 847, 70
Quimby, R. M., Oguri, M., More, A., et al. 2014, *Science*, 344, 396
Shen, Y., Richards, G. T., Strauss, M. A., et al. 2011, *ApJS*, 194, 45
Skrutskie, M. F., Cutri, R. M., Stiening, R., et al. 2006, *AJ*, 131, 1163
Sugimura, K., Hosokawa, T., Yajima, H., Inayoshi, K., & Omukai, K. 2018, *MNRAS*, 478, 3961
Trakhtenbrot, B., Lira, P., Netzer, H., et al. 2017, *ApJ*, 836, 8
Turner, E. L. 1980, *The Astrophysical Journal*, 242, L135
Venemans, B. P., Neeleman, M., Walter, F., et al. 2019, *ApJ*, 874, L30
Venemans, B. P., Findlay, J. R., Sutherland, W. J., et al. 2013, *ApJ*, 779, 24
Venemans, B. P., Verdoes Kleijn, G. A., Mwebaze, J., et al. 2015, *MNRAS*, 453, 2259
Venemans, B. P., Decarli, R., Walter, F., et al. 2018, *ApJ*, 866, 159
Vestergaard, M., & Osmer, P. S. 2009, *ApJ*, 699, 800
Volonteri, M., & Rees, M. J. 2006, *ApJ*, 650, 669
Walter, F., Riechers, D., Novak, M., et al. 2018, *ApJ*, 869, L22
Wang, F., Wang, R., Fan, X., et al. 2019, arXiv e-prints, arXiv:1906.06801
Wang, R., Wagg, J., Carilli, C. L., et al. 2013, *ApJ*, 773, 44
Willott, C. J., Delorme, P., Reylé, C., et al. 2010, *AJ*, 139, 906
Wright, E. L., Eisenhardt, P. R. M., Mainzer, A. K., et al. 2010, *AJ*, 140, 1868
Wu, X.-B., Wang, F., Fan, X., et al. 2015, *Nature*, 518, 512
Wyithe, J. S. B., & Loeb, A. 2002, *Nature*, 417, 923
York, D. G., Adelman, J., Anderson, Jr., J. E., et al. 2000, *AJ*, 120, 1579